



## **25 years of field exposure of pre-cracked concrete beams; combined impact of spacers and cracks on reinforcement corrosion**

**Geiker, Mette ; Danner, Tobias; Michel, Alexander; Belda Revert, Andres; Linderoth, Oskar; Hornbostel, Karla**

*Published in:*  
Construction and Building Materials

*Link to article, DOI:*  
[10.1016/j.conbuildmat.2021.122801](https://doi.org/10.1016/j.conbuildmat.2021.122801)

*Publication date:*  
2021

*Document Version*  
Publisher's PDF, also known as Version of record

[Link back to DTU Orbit](#)

*Citation (APA):*  
Geiker, M., Danner, T., Michel, A., Belda Revert, A., Linderoth, O., & Hornbostel, K. (2021). 25 years of field exposure of pre-cracked concrete beams; combined impact of spacers and cracks on reinforcement corrosion. *Construction and Building Materials*, 286, Article 122801. <https://doi.org/10.1016/j.conbuildmat.2021.122801>

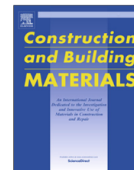
---

### **General rights**

Copyright and moral rights for the publications made accessible in the public portal are retained by the authors and/or other copyright owners and it is a condition of accessing publications that users recognise and abide by the legal requirements associated with these rights.

- Users may download and print one copy of any publication from the public portal for the purpose of private study or research.
- You may not further distribute the material or use it for any profit-making activity or commercial gain
- You may freely distribute the URL identifying the publication in the public portal

If you believe that this document breaches copyright please contact us providing details, and we will remove access to the work immediately and investigate your claim.



# 25 years of field exposure of pre-cracked concrete beams; combined impact of spacers and cracks on reinforcement corrosion

Mette Geiker<sup>a,\*</sup>, Tobias Danner<sup>a,b</sup>, Alexander Michel<sup>c</sup>, Andres Belda Revert<sup>a</sup>, Oskar Linderroth<sup>d</sup>, Karla Hornbostel<sup>e</sup>

<sup>a</sup> Department of Structural Engineering, Norwegian University of Science and Technology (NTNU), Trondheim, Norway

<sup>b</sup> SINTEF Community, Architecture, Materials and Structures, Trondheim, Norway

<sup>c</sup> Department of Civil Engineering, Technical University of Denmark, Kgs. Lyngby, Denmark

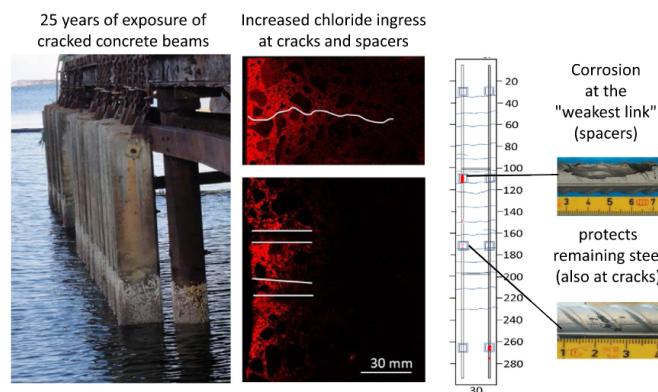
<sup>d</sup> Division of Building Materials, Lund University, Lund, Sweden

<sup>e</sup> Operations and Maintenance, Norwegian Public Roads Administration (NPRA), Trondheim, Norway

## HIGHLIGHTS

- Increased ingress at cracks in 25 years old marine concrete.
- Severe corrosion in connection with plastic spacers, none or negligible at cracks.
- Corrosion at the “weakest link” appears to protect the remaining steel.

## GRAPHICAL ABSTRACT



## ARTICLE INFO

### Article history:

Received 13 July 2020

Received in revised form 19 February 2021

Accepted 21 February 2021

### Keywords:

Reinforced concrete

Cracks

Spacers

Long-term marine exposure

Reinforcement corrosion

## ABSTRACT

The state of corrosion of three pre-cracked concrete beams was investigated after 25 years of marine exposure (atmospheric, tidal and submerged). The influence of inadequate plastic spacers was found to overrule the possible impact of bending cracks on reinforcement corrosion. Increased chloride ingress was detected in cracked areas, but very little corrosion was observed where cracks reached the reinforcement. Also, high chloride content was measured in uncracked parts of the beams, but no or very limited corrosion was observed outside spacers and a few cracks. It is hypothesised that corrosion, initiated early at weak spots (here at plastic spacers) can protect the remaining reinforcement from corrosion.

© 2021 The Authors. Published by Elsevier Ltd. This is an open access article under the CC BY license (<http://creativecommons.org/licenses/by/4.0/>).

\* Corresponding author.

E-mail address: [mette.geiker@ntnu.no](mailto:mette.geiker@ntnu.no) (M. Geiker).

<https://doi.org/10.1016/j.conbuildmat.2021.122801>

0950-0618/© 2021 The Authors. Published by Elsevier Ltd.

This is an open access article under the CC BY license (<http://creativecommons.org/licenses/by/4.0/>).

## 1. Introduction

There is consensus that cracks promote the ingress of carbon dioxide and chloride, and thus facilitate initiation of reinforcement corrosion, see e.g. [1–3]. However, there is no agreement on the extent to which cracks shorten the initiation period [1]. Based on especially the mentioned references, we earlier [4] summarized that (i) short-term investigations (up to a few years) indicate that corrosion rates are enhanced by cracks and mainly depend on cover depth and concrete quality rather than on crack width, and that (ii) the few available long-term studies indicate that smaller cracks (<0.5 mm) have limited influence on long-term corrosion propagation. Depending on the moisture content, cracking also facilitates transport of water and/or oxygen into the concrete.

A recent literature review [1] illustrates the impact of cover depth on reported threshold crack widths below which cracks are considered unimportant for reinforcement corrosion. An explanation for the impact of cover depth could be that low cover depth increases the impact of exposure and thus the probability of moisture variations at the steel–concrete interface. Already in 1982 Tuutti [5] suggested that moisture and temperature variations at the steel surface facilitate corrosion initiation. This was later supported by others as summarised in a recent review by RILEM TC 262 SCI (steel–concrete interface) [6]. Low cover depth also increases the likelihood of possible leaching at the steel–concrete interface, thereby lowering the pH of the pore solution surrounding the steel and increasing the susceptibility of the steel to chloride ions.

Different types of self-healing are the general hypotheses for reduced corrosion propagation or even re-passivation over time. In marine exposed concrete precipitation of magnesium hydroxide and calcium carbonate in cracks is typically observed [7,8]. Observations of extensive precipitation of solids in marine exposed cracks of width up to 0.2 mm and in some cases wider indicate that the potential impact of cracks on transport may gradually cease, see e.g. [9].

Due to the non-conclusive and limited results from field exposed structures, and the impact of crack width limitations on the structural detailing and costs of projects, a research project was in 2015 initiated within the Norwegian Public Roads Administration's R&D program "Ferry-free coastal route E39". A main part of the project was the collection of long-term field data on the influence of cracks on chloride ingress and reinforcement corrosion. It was found that the impact of cracks varies greatly depending on the orientation and exposure [10]. Cores extracted from cracked areas in edge beams of two de-iced bridges in Trondheim, one road tunnel in Oslo, and the splash zone of three marine exposed concrete elements support the ranking of the impact of cracks suggested in the *fib* Model Code for service life design [11]. Horizontal ponding was found most aggressive, followed by exposure of a horizontal crack on a vertical surface, to exposure of a vertical crack on a vertical surface [12]. Chloride ingress is of main concern, but possible carbonation of the steel–concrete interface causing a major pH drop and thus increasing the sensitivity to chloride ions as well as the corrosion rate should also be considered [12].

This paper presents investigations of the state of corrosion in three pre-cracked concrete beams exposed for 25 years in marine submerged, tidal and atmospheric zones. The investigations covered chloride content, moisture content, concrete resistivity, half-cell potentials and extent of corrosion. Investigations of self-healing of cracks have been published in a separate paper [9]. The beams differed in binder composition, and the width of the cracks introduced by 3-point bending varied over the length with in general largest crack width at the centre of the beam positioned

in the tidal zone. We found that the steel in the vicinity of the spacers used was most susceptible to corrosion and it was hypothesised that corrosion sustained at these "weak spots" resulted in reduced susceptibility of the steel to chlorides in other areas by providing cathodic polarisation.

## 2. Field station and beams

The present investigations cover three 25-year-old marine exposed pre-cracked concrete beams. The beams were part of a larger testing programme established by the Norwegian Public Road Administration (NPRA) in 1993. Concrete elements were exposed at four different field sites in Norway, Field Station Sandnessjøen being one of them. Elements of in total 17 different concrete compositions were prepared [13].

This investigation covered three cracked beams (no uncracked beams were available for reference). The beams were cast lying horizontally on the side providing similar conditions for the reinforcement and spacers along the beams [13]. The cracks were introduced by 3-point bending. Right after loading the beams in 1993, the distance between the cracks was 100–150 mm, the crack depth of 70–90 mm, and the crack width 0.1–0.2 mm [13]. The cracks were maintained by coupling two beams in 3-point bending. More details on the loading of the concrete beams can be found in the report from Holtmon and Isaksen [13].

The beams were mounted from a quay near Sandnessjøen (Fig. 1). The mean water level is about at the middle of the beams; and the tidal changes are between  $\pm 0.5$  and  $\pm 1.4$  m (tide-forecast, no) [14]. Information on temperature and precipitation can be obtained from yr.no and no.climate-data.org, respectively. In 2017 the minimum and maximum temperatures were  $-10$  and  $24$  °C, and the average temperature during the coldest and warmest month was  $-2$  °C and  $16$  °C, respectively. The monthly precipitation was 100–267 mm. The composition of the seawater (Atlantic Sea) is according to [15] 19,000 mg/L chlorine, 10,500 mg/L sodium, 1350 mg/L magnesium, 890 mg/L sulfur, 400 mg/L calcium, 380 mg/L potassium, and 28 mg/L carbon.

## 3. Experimental investigation

### 3.1. Materials

The concrete compositions are given in Table 1. Three concrete compositions were investigated, one in accordance with today's NPRA requirements (E), one used during the 80's and 90's (B) and a more extreme composition with a high silica fume content (F). The composition of the binders is given in Table 2. SEM-EDS point analyses showed that the concretes containing only silica fume as supplementary material (Beam B and Beam F) were rather similar in paste composition which mainly consisted of C–S–H with calcium hydroxide and AFm phases, whereas the concrete also containing fly ash (Beam E) differed somewhat in paste composition [9,16]. In general, the paste in Beam E had a higher Al/Ca and Si/Ca ratio compared to the two other concretes, resulting in a lower C–S–H content [9,16].

The location and numbering of cores and the nomenclature used are illustrated in Fig. 2. The concrete beams had a dimension of  $300 \times 30 \times 15$  cm with truncated corners. Ribbed reinforcement bars with 16 mm diameter were used. One U-bended rebar providing two parallel legs (corresponding to Line 2 and Line 3 in Fig. 2) was used in each beam. As mentioned in Section 2, the beams were cast lying horizontally; the rebar in Line 2 was top-bar in Beams B and E, but bottom-bar in Beam F. The U-bend was facing up (in the atmospheric zone) where the beams were fastened; the bend is not



Fig. 1. Beams at Field Station Sandnessjøen.

**Table 1**  
Concrete compositions [17].

Component	Unit	Beam B	Beam E	Beam F
Cement (c)	kg/m <sup>3</sup>	373	384	398
Silica fume (sf)	% (bwc) <sup>b</sup>	4	4	12
Fly ash (fa) <sup>a</sup>	% (bwc) <sup>b</sup>	0	(20)	0
Free water (w)	kg/m <sup>3</sup>	160.5	166.6	198.7
Aggregate 0–8 mm	kg/m <sup>3</sup>	928	1014	881
Aggregate 8–16 mm	kg/m <sup>3</sup>	904	820	841
Air entrainer	kg/m <sup>3</sup>	0.3	0.6	0
Plasticizer	kg/m <sup>3</sup>	6.0	7.9	8.5
Paste volume	%	28.6	29.5	34.8
Theoretical density	kg/m <sup>3</sup>	2384	2401	2371
Equivalent w/c <sup>a</sup>	–	0.40	0.40	0.40

<sup>a</sup> Equivalent w/c =  $w/(c+(k_{sf} \cdot sf))$ ;  $k_{sf} = 2$ . The fly ash was intermixed with the cement at the cement plant and thus part of the cement and given efficiency factor,  $k_{fa} = 1$ . The resulting fly ash cement was called CEM II, MP30.

<sup>b</sup> bwc: by weight of cement.

**Table 2**  
Composition of cement (CEM I, P30 Norcem), fly ash and silica fume (composition of fly ash and silica fume used in parallel project [18]).

Oxides	Unit	CEM I	Fly ash	Silica fume
CaO	wt%	63.3	3.6	0.1
SiO <sub>2</sub>	wt%	20.6	55.4	95.1
Al <sub>2</sub> O <sub>3</sub>	wt%	4.8	27.4	1.0
Fe <sub>2</sub> O <sub>3</sub>	wt%	3.5	3.9	0.1
MgO	wt%	2.2	1.0	0.4
SO <sub>3</sub>	wt%	2.8	N/A	0.0
K <sub>2</sub> O	wt%	1.0	1.1	1.0
Na <sub>2</sub> O	wt%	0.35	0.3	0.1
LOI	wt%	1.0	N/A	N/A
Specific surface area	m <sup>2</sup> /kg	341	N/A	N/A

N/A = not available.

shown in the sketches. As indicated in Fig. 2, two connections were placed at approximately 100 and 200 cm from the top. These connections were placed beneath the main reinforcement and therefore had a larger cover. The connections were welded to the main reinforcement. The prescribed concrete cover to the main reinforcement was 25 mm from the cracked (“top”) side and 75 mm from the adjacent shorter sides. The position of the reinforcement in the concrete beams was located with a cover meter and later checked with excavating the rebars. The measured concrete cover was in agreement with the drawings. Plastic spacers (see Fig. 12, c) were used from the top side (25 mm cover) to keep the reinforcement in place during casting of the beams. The beams were taken out of water, partially cleaned from seashells, packed tightly in thick plastic and transported on an open truck to Trondheim on 14th March 2018. The following day, before moving the

beams into the laboratory, remaining seashells and algae were scratched off the surface with a big spatula and the beams were cleaned with water using a pressure washer.

### 3.2. Experimental methods

#### 3.2.1. Visual inspection

The visual inspection included documentation of crack pattern and the location of spacers, spalling, and precipitations.

#### 3.2.2. Cover measurements

A cover meter from Proceq (Profometer) was used to locate the reinforcement in the concrete beams. The location of the reinforcement was drawn on the concrete surface to support later measurements of half-cell potential, concrete resistivity and surface crack



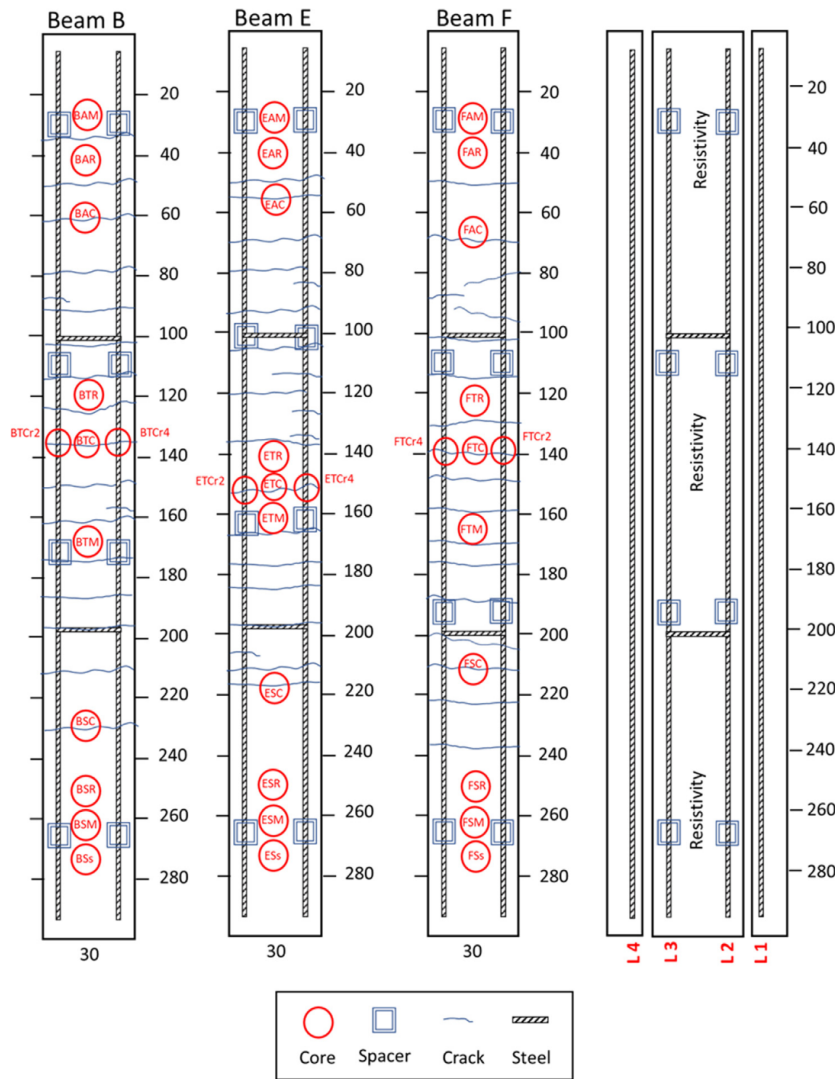


**Fig. 2.** Location and numbering of; left: cores and right: lines for half-cell potential (L1, L2, L3 and L4) and surface resistivity measurements. Distance from the top and width in cm.

widths. The cover measurements were checked when opening the beams.

### 3.2.3. Crack width measurements

The crack widths were measured with a crack width ruler before unloading the beams. The crack width ruler had intervals of 0.05 mm above 0.1 mm, and intervals of 0.025 mm below 0.1 mm. It was difficult to differentiate between 0.075 and 0.1 when measuring visually. The crack widths were measured along all four lines (L1, L2, L3, L4) (Fig. 2) and in between lines L3 and L4. The crack patterns and surface crack widths were documented in crack maps.

### 3.2.4. Half-cell potential measurement

Half-cell potential measurements (HCP) were performed above the reinforcement according to [19] using a Profometer wheel electrode collecting data points every 5 cm. The potential was mapped

above the reinforcement of the concrete beams along lines L1, L2, L3 and L4 (see Fig. 2). A copper/copper sulphate electrode was used. To check the accuracy of the wheel electrode, the potential difference between the wheel electrode and a rod electrode (as well CSE) was measured. The difference was 3 mV which is considered negligible.

### 3.2.5. Resistivity measurement

Resistivity measurements were performed at selected areas of 40 cm × 10 cm on the top surface of the concrete beams in the, atmospheric zone (20–60 cm), tidal zone (120–160 cm) and submerged zone (240–280 cm) (see Fig. 2). The measurements were taken between reinforcement (between Line L2 and Line L3) at approx. 20 °C in the laboratory using a Proceq Resipod Wenner probe (4-electrode setup, 50 mm probe spacing). Twenty (20) resistivity measurements were taken and the average value was calculated.

Additional resistivity measurements were performed on concrete cores (-R) according to [20]. Metal plates were placed on the two flat ends of the concrete cores with moist cloths between the metal plates and the concrete surfaces. Tap water was used as contact solution. The electrode plates were coupled to an Agilent LCR meter and measurements were taken with a frequency of 100 and 120 Hz, 1 and 10 kHz. For each core, the value with the lowest phase angle was used [21]. Measurements were taken at  $5 \pm 1$  °C in the cooling room where the concrete cores were stored.

According to Polder [22] a temperature increase causes a decrease of resistivity and vice versa. The temperature effect may vary with moisture content, laboratory data indicate a resistivity change of 3% for saturated and 5% for dry concrete for each degree Celsius change [22].

### 3.2.6. Chloride profiles measurement

Profile grinding and chemical analysis were performed according to [20]. The layer thickness for profile grinding was 0–3, 3–6, 6–10, 10–15, 15–20, 20–30, 30–40, 40–50 mm. About 5 g of the concrete powder from each layer were dried overnight at 105 °C. The dried powder was dissolved in 50 ml 80 °C (1:10)  $\text{HNO}_3$  and filtrated after 1 h. The chloride content in the filtrated solution was determined by potentiometric titration with a Titrand 905 titrator from Metrohm using 0.01 M  $\text{AgNO}_3$ .

### 3.2.7. Elemental mapping using $\mu$ -XRF

$\mu$ -XRF elemental mapping and qualitative determination of chloride ingress was performed using a M4 Tornado from Bruker according to [23]. Elemental mapping was performed at 50 kV accelerating voltage and 600  $\mu\text{A}$  with a silver X-Ray tube. Two silicon drift detectors were used simultaneously for fast data collection. Elemental mapping was performed with 80  $\mu\text{m}$  distance between each pixel and 1 ms/pixel collection time. The whole area of the taken concrete cores was mapped, i.e. 95 mm x 150 mm and 70 mm x 150 mm. Note that intensities are relative to the maximum intensities detected in each individual map.

### 3.2.8. Moisture characterization, degree of capillary saturation and relative humidity

Concrete cores of 100 mm diameter and 150 mm length were taken from all three exposure zones of each concrete beam. The concrete cores were split in three slices of approximately 50 mm thickness each. In a third step, each slice was split further into four parts. All steps were undertaken fast to reduce disturbance of the sample during subdivision.

Degree of capillary saturation (DCS) measurements were performed according to [20]. The following procedure was applied:

1. Splitting of concrete cores
2. Weighing of samples directly after splitting
3. Submersion in water and weighing saturated surface dry in air after 21 days to determine the suction capacity
4. Drying at 105 °C for 7 days
5. Submersion in water and weighing saturated surface dry in air and in water after 7 days to determine the volume.

The relative humidity (RH) was measured by SINTEF as described by Lindgård et al. [24]. For measurements of RH the samples were crushed into smaller pieces (max 5 mm). Aggregates were to the extent possible separated from the cement paste and discharged. The remaining grains of mainly cement paste were transferred into a test tube, filling half of the tube, which was closed by mounting a RH sensor and sealing the opening with parafilm. The closed tube was placed in an isolated box in a climate-controlled room (20 °C). Readings were performed daily for

approximately a week, and the maximum value was used. For most of the samples the maximum value was observed after a few days of equilibration; however, for unknown reasons some of the samples showed decreasing RH from the beginning (BAM, BTM, FAM). The RH was measured with calibrated Vaisala sensors "HM44". The reported accuracy of the sensors is  $\pm 2\%$  in the range of 0–90% RH and  $\pm 3\%$  in the range of 90–100% RH [25].

### 3.2.9. Sorption balance measurements

For each sorption balance measurement, a few grams of material were extracted from the centre part of the submerged cores BSs, ESs, FSs. The material was crushed using a mortar and pestle (maximal particle size approximately 1 mm) after which a generous amount of deionized water was added covering the sample. The moist material was then placed in 20 ml plastic vials, sealed with tight plastic lids, for 24 h before the start of the sorption balance measurements.

Desorption isotherms were measured on approximately 80 mg samples of the crushed and water saturated material using a DVS 1000 (BSs) and two DVS Intrinsic (ESs, FSs) sorption balances from Surface Measurement Systems, UK. In these instruments, the mass of a sample is continuously measured with an analytical balance during exposure to a pre-determined RH, see e.g. Williams [26]. The desired RH is achieved by a mixture of saturated water vapour and dry nitrogen gas. The RH of the sorption balances was validated by measurements on saturated salt solutions according to the method described by Wadsö et al. [27] and found to vary  $\pm 1.5\%$  from the set values.

In this study, a RH-program consisting of nine steps between 95 and 11% RH was used. The steps and their durations are given in Appendix 1. The isotherms were derived from the final measured mass at each step, see [28]. The upper RH-limit at 95% is an experimental constraint as at higher RHs water may condense inside the instrument. The lower RH-limit, i.e. the dry state, was defined as mass equilibrium at 11% RH. According to Feldman and Ramachandran [29,30] further drying will result in a significant loss of chemically bound water. However, some loss of chemically bound water will have occurred already at 30% RH [31]. The desorption isotherms are expressed as mass of evaporable water ( $W_e$ ) per gram of binder (B), where dividing by the latter made it possible to compare the desorption isotherms of the different concretes. The binder content of each sample was calculated from the calcium content as measured by inductively coupled optical emission spectroscopy (ICP-OES), according to the method described by Linderoth & Johansson [32].

### 3.2.10. Excavation of reinforcement, characterization of pits and estimation of corrosion rate

The concrete was completely removed from the reinforcement to determine the extent of corrosion. The concrete was cut from the back (side wide large cover) with a concrete saw until about 0.5 cm above the reinforcement and then carefully split with hammer and chisel. The rebars were cleaned by sandblasting before characterising pits. Fig. 12 shows examples of rebars before and after cleaning.

Corrosion pits were characterized by measuring their maximum depth and length. The corrosion rate was calculated based on two assumptions: a) maximum pit depth being representative for the whole length of the anodic site, b) constant corrosion development during the entire exposure period (25 years). The first assumption leads to an overestimation of the corrosion rate, while the latter assumption leads to an underestimation, and the calculations should therefore only be taken as indicative. Further details can be found in [21].

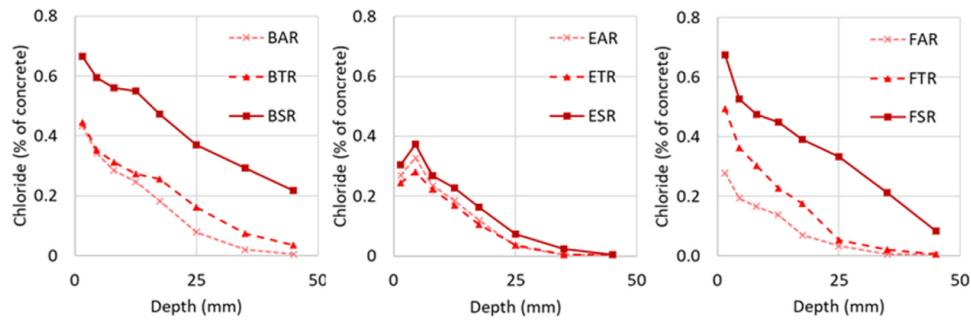


**Fig. 3.** Chloride profiles measured in the atmospheric, tidal and submerged zones of Beam B, Beam E and Beam F. The vertical gridline at 25 mm coincides with the cover depth.

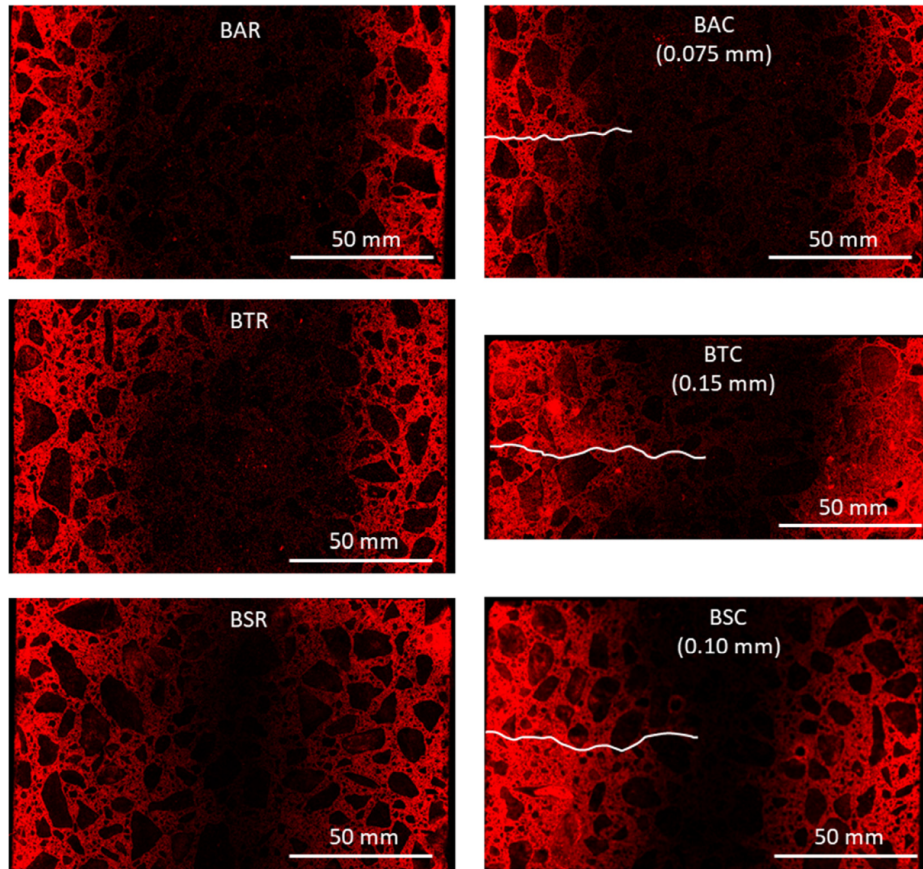
#### 4. Experimental results

The results of the experimental investigations are summarized below. Raw data can be found in the data report prepared by Danner et al. [21]. Data on self-healing were given and discussed by Danner et al. in [9].

The beams contained multiple horizontal cracks of maximum width 0.20 mm (Beams B and Beam F) and 0.35 mm (Beam E). Spal-

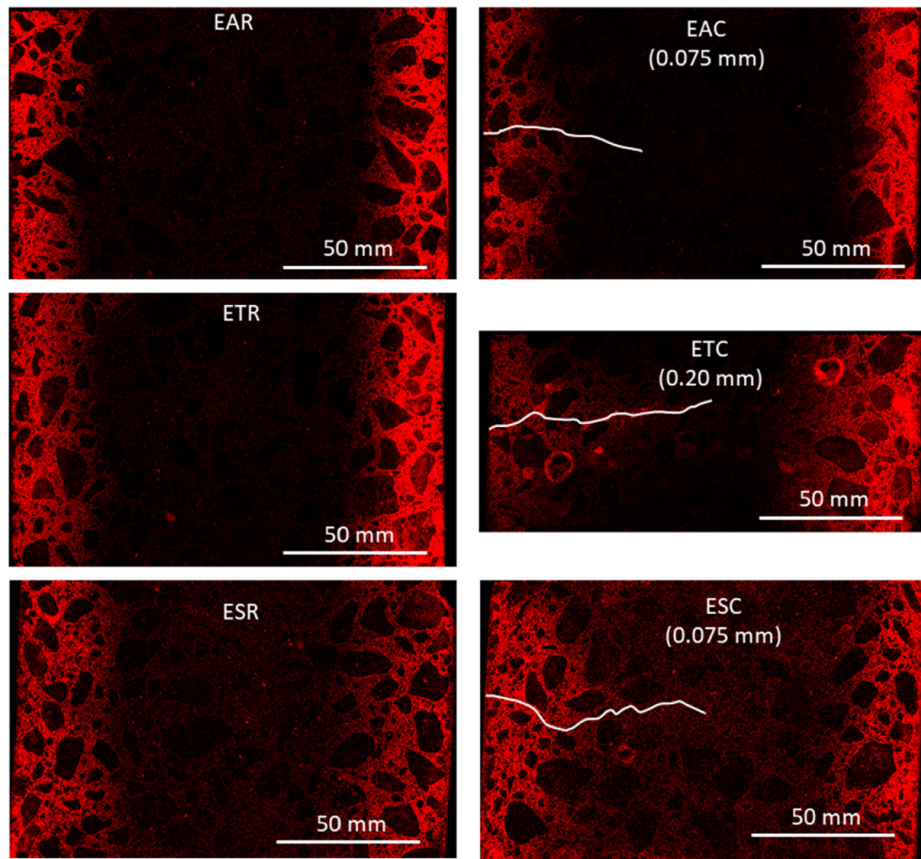
ling was observed at one spacer in Beam B and at three spacers in Beam F. Maps of the visual appearance of the three beams are given in the Appendix 2.

Fig. 3 shows the chloride profiles of concrete cores taken between cracks from Beams B, E and F from the atmospheric (cores BAR, EAR, FAR), tidal (cores BTR, ETR, FTR) and submerged (cores BSR, ESR, FSR) zones. Tabulated values can be found in the data report prepared by Danner et al. [21]. In all three concrete beams,



**Fig. 4.**  $\mu$ -XRF chloride maps of left: reference cores (BAR, BTR, BSR) and right: cores with cracks (BAC, BTC, BSC) from the three exposure zones of Beam B. Surface crack widths are indicated in brackets. Each picture is normalized to the highest measured intensity within the picture. The mapping area was slightly larger than the whole width of the core causing black stripes on the left and right sides in some maps.





**Fig. 5.**  $\mu$ -XRF chloride maps of left: reference cores (EAR, ETR, ESR) and right: cores with cracks (EAC, ETC, ESC) from the three exposure zones of Beam E. Surface crack widths are indicated in brackets. Each picture is normalized to the highest measured intensity within the picture. The mapping area was slightly larger than the whole width of the core causing black stripes on the left and right sides in some maps.

the deepest chloride ingress was measured in the submerged zone. However, for Beam E, little difference in chloride ingress was observed between the three zones, which might be explained by comparable surface concentrations and relatively low and comparable moisture contents, especially in the tidal and submerged zones (see Fig. 10). In total, there was less chloride ingress measured in Beam E. The profiles from shorter exposure times given in Appendix 3 show similar limited difference in chloride ingress in the three exposure zones.

In Fig. 4, Fig. 5 and Fig. 6 the chloride maps measured with  $\mu$ -XRF on uncracked reference cores (-R) and cores with cracks (-C) from Beam B, Beam E and Beam F are shown. The chloride maps show gradients of intensities from the surfaces to the centre. Note that each picture is normalized to the highest intensity within the picture as intended calibration did not allow sufficient quantification. Thus, unless comparable concrete composition and exposure, different pictures should not be directly compared regarding intensities of chloride. Concrete cores were drilled through the beam; therefore, chloride ingress is visible from both sides of the concrete cores.

All concrete beams were mounted as pairs on the ferry quay near Sandnessjøen. The left side in Fig. 4, Fig. 5 and Fig. 6 represents the cracked “top side” of the beams. The right side represents the “bottom side” of the beams, oriented towards the other con-

crete beam of each pair. No systematic difference in chloride ingress from top and bottom sides was observed.

Considering that the surface concentrations in the atmospheric zone were lower or equal to the surface concentrations measured in the tidal and submerged zone (see Fig. 3) and that the minimum concentration (detection limit) should be the same for all scans, the  $\mu$ -XRF scans confirm that for all concrete beams the chloride ingress depth is increasing from the atmospheric to the submerged zone (see Fig. 4, Fig. 5 and Fig. 6).

In some cases, a deeper ingress of chlorides is observed along cracks when compared to the chloride ingress of the reference cores without cracks, see Fig. 4, Fig. 5 and Fig. 6, left hand side cores without cracks (-R), right hand side cores with cracks (-C). Especially, the cores from the tidal zone (BTC, ETC, FTC) having the widest cracks show an impact of the cracks on chloride ingress.

As a general observation, a white precipitate was observed on the reinforcement and the imprint in the concrete near cracks when removing the concrete from the reinforcement; an example is shown in Fig. 7a.  $\mu$ -XRF elemental mapping showed increased chloride and sulphate content in areas with the white precipitate (Fig. 7b, c), and SEM-EDS point analysis indicated that the white precipitate was ettringite [16].

Water vapour sorption isotherms for the three types of concrete are given in Fig. 8. The data are tabulated in Appendix 1. Beam F



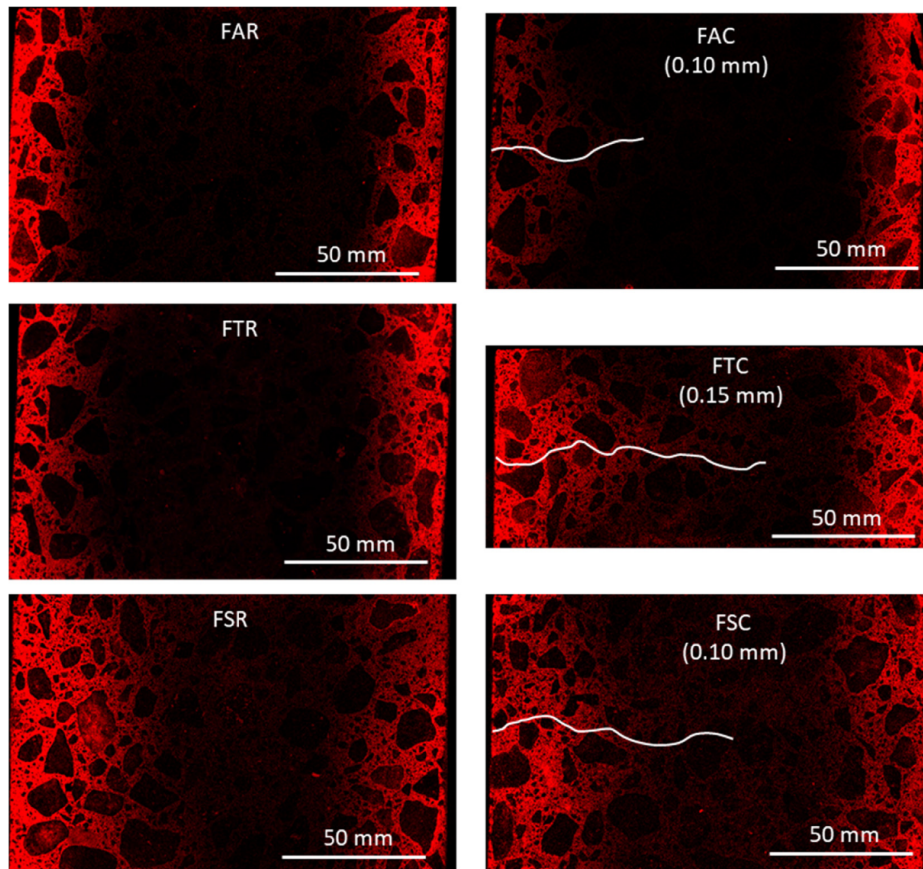


**Fig. 6.**  $\mu$ -XRF chloride maps of left: reference cores (FAR, FTR, FSR) and right: cores with cracks (FAC, FTC, FSC) from the three exposure zones of Beam F. Surface crack widths are indicated in brackets. Each picture is normalized to the highest measured intensity within the picture. The mapping area was slightly larger than the whole width of the core causing black stripes on the left and right sides in some maps.

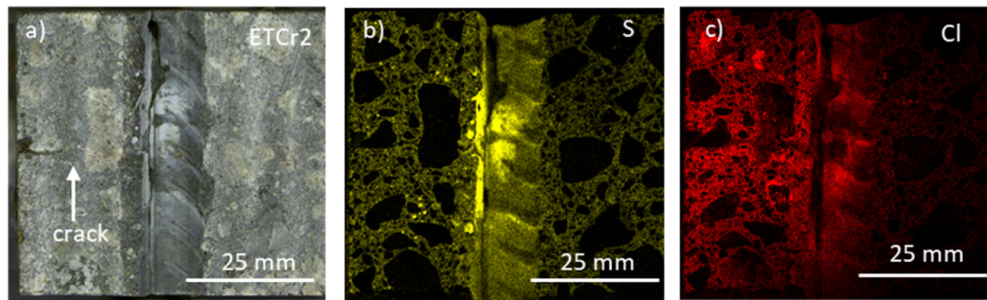


**Fig. 7.** Cracked core with imprints from removed reinforcement. a) White precipitate at reinforcement imprint in the concrete near crack. b) and c)  $\mu$ -XRF elemental chloride and sulphate mapping. Beam E, line 2, 150 cm from the top.

(with the high silica fume content) had a higher fine porosity, indicating a relative higher amount of C-S-H, and in the hygroscopic range measured a total higher porosity. Beam E (with fly ash) had a relative higher volume of coarser pores indicated by the steeper slope in the high RH range. Similar observations of higher coarser porosity of fly ash containing paste were made by Linderoth testing samples up to 1.5 years [28], however only in samples with high fly ash content (35%). Despite the coarser pore structure,

decreasing water vapour transport was found with increasing fly ash content indicating change in the morphology of paste [28].

Fig. 9, Fig. 10 and Fig. 11 summarize for each of the three beams the measured half-cell potential, the concrete resistivity of the surface concrete ( $\rho_{\text{beam}}$  measured at approximately 20 °C) and the bulk concrete ( $\rho_{\text{core}}$  measured on extracted cores kept at 5 °C), the degree of capillary saturation (DCS) and the relative humidity (RH) of the 0–50 ± 10 mm slice from the exposed surface, the chlo-

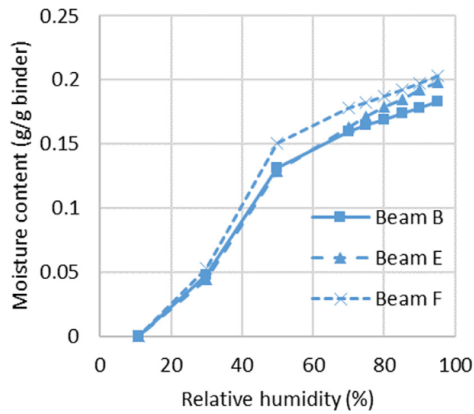


Fig. 8. First desorption isotherms. Moisture content per gram of binder at each relative humidity step as well as the duration of each step. Reference at 11%.

ride content at the reinforcement (samples collected 20–30 mm from the exposed surface) and the extent of corrosion observed

on reinforcement after removal of concrete and cleaning of the reinforcement. Tabulated values can be found in the data report prepared by Danner et al. [21].

An overview of the observed corrosion pits is given in Appendix 4. Examples of severe pitting corrosion at a spacer in the tidal zone of Beam B (location at around 110 cm at Line 2) and distributed pitting at a spacer in the tidal zone of Beam E (location at around 160 cm at Line 2) are shown in Fig. 12.

Based on the size of the corrosion pits (using maximum length and depth; see Section 2) and assuming a constant corrosion rate during the entire 25 years, corrosion rates between less than 1 and 60  $\mu\text{m}/\text{year}$  were estimated (Appendix 4). High corrosion rates were only observed at spacers in the tidal and submerged zone, but not at all spacers. The only corrosion spot not coinciding with a spacer or a crack was not related to a visible void.

$\mu\text{-XRF}$  elemental mapping of chloride, magnesium and sulphur at a spacer (Beam B, location at around 110 cm at Line 2) is shown in Fig. 13. The chloride map shows increased chloride ingress along the spacer. The magnesium map indicates a high ingress of seawater. The sulphur map indicates a high moisture load (causing dissolution and reprecipitation of sulphur rich phases) and potential seawater ingress.

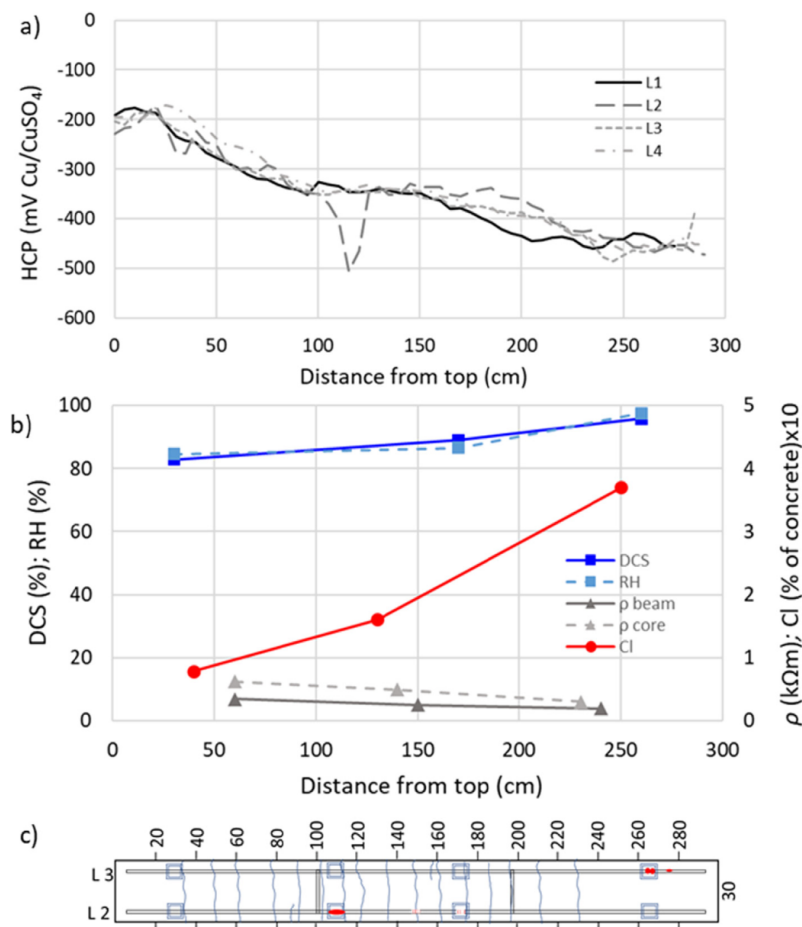
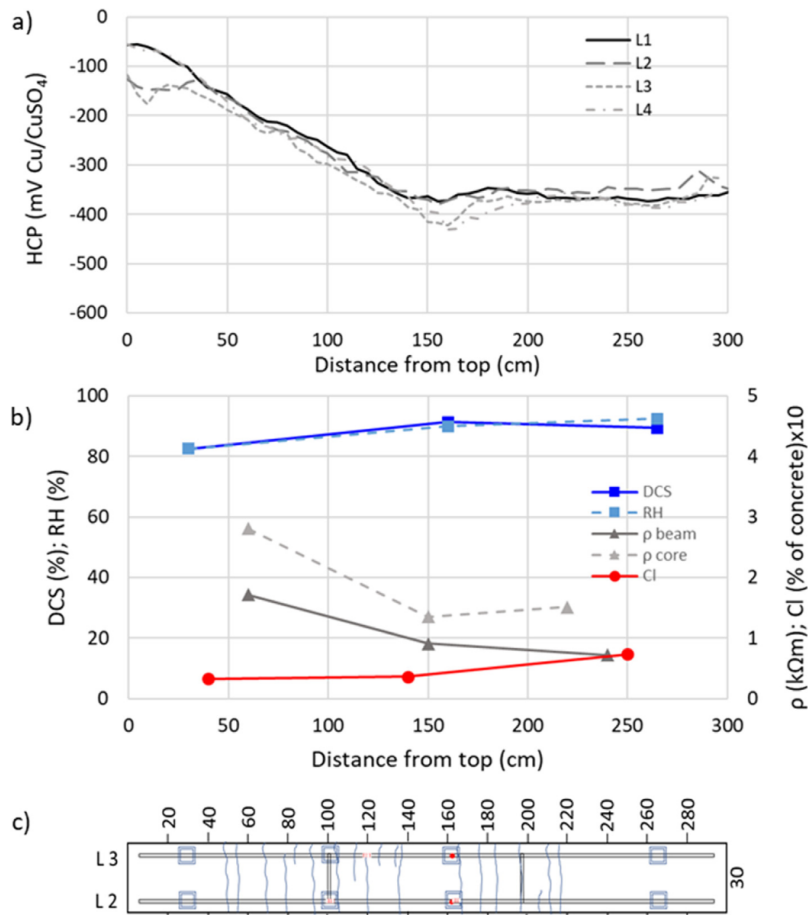


Fig. 9. Beam B. a) half-cell potential, b) degree of saturation (DCS), relative humidity (RH), surface and bulk resistivity ( $\rho_{\text{beam}}$  and  $\rho_{\text{core}}$ , not temperature compensated) and chloride content at rebar, and c) extent of corrosion observed on reinforcement after removal of concrete and cleaning of rebars (marked in red). Length measures in cm. (For interpretation of the references to colour in this figure legend, the reader is referred to the web version of this article.)



**Fig. 10.** Beam E. a) half-cell potential, b) degree of saturation (DCS), relative humidity (RH), surface and bulk resistivity ( $\rho_{\text{beam}}$  and  $\rho_{\text{core}}$ , not temperature compensated) and chloride content at rebar, and c) extent of corrosion observed on reinforcement after removal of concrete and cleaning of rebars (marked in red). Length measures in cm. (For interpretation of the references to colour in this figure legend, the reader is referred to the web version of this article.)

## 5. Discussion

The focus of this study is the long-term impact of cracks on the corrosion performance of the embedded reinforcement. Data for the general properties of the beams (resistivity, chloride ingress, moisture state) are given to provide background for this. To keep the focus of the paper, we have by purpose limited the discussion of the individual parameters here. The measured chloride profiles are supported by unpublished data for ingress after 2.5, 10 and 21 years (see Appendix 3) performed by NPRA. For Beam F, the profiles are varying, and especially the measured ingress in the submerged zone is unexpected deep and large (see Appendix 3). Concerning the half-cell potential and resistivity data, unpublished data from NPRA show similar trends for concrete beams exposed at NPRA's field exposure station at Solsvik near Bergen, Norway [33].

For the investigated beams with a cover depth of 25 mm, the threshold crack width below which cracks are considered unimportant for reinforcement corrosion based on literature data summarised by Käthler et al. [1] is in the range 0.1–0.2 mm. Surface crack width above 0.1 mm were observed in all beams, whereas surface crack width above 0.2 mm were only observed on Beam E (3 cracks) and Beam F (1 crack).

The observed correlation between crack width, spacers and calculated corrosion rate is illustrated in Fig. 14. In general, very limited corrosion was observed outside spacers despite cracks and high chloride content. Observations on all three beams after 25 years marine exposure show:

- Corrosion at some spacers, especially in the tidal zone (see Fig. 9, Fig. 10 and Fig. 11)
- Increased chloride ingress at cracks (see Fig. 4, Fig. 5 and Fig. 6), but very little corrosion at cracks
- High chloride content in the submerged parts of Beams B and F (see Fig. 3), but no or very limited corrosion outside spacers and a few cracks.

Estimated corrosion rates at spacers, cracks and in bulk are given in Appendix 4. The estimates are based on observed corrosion pits after 25 years.

### 5.1. Corrosion outside spacers and cracks

Corrosion outside cracks and spacers was only observed in one beam and at one location (Beam B, line 4, 275 cm). This location



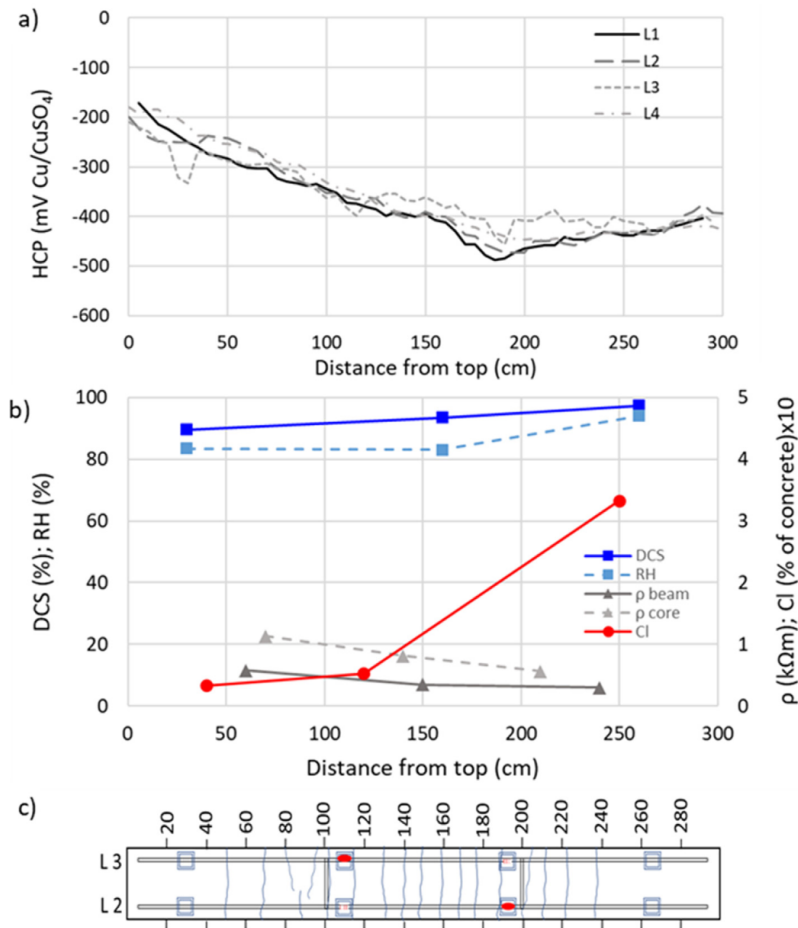


**Fig. 11.** Beam F. a) half-cell potential, b) degree of saturation (DCS), relative humidity (RH), surface and bulk resistivity ( $\rho_{\text{beam}}$  and  $\rho_{\text{core}}$ , not temperature compensated) and chloride content at rebar, and c) extent of corrosion observed on reinforcement after removal of concrete and cleaning of rebars (marked in red). Length measures in cm. (For interpretation of the references to colour in this figure legend, the reader is referred to the web version of this article.)

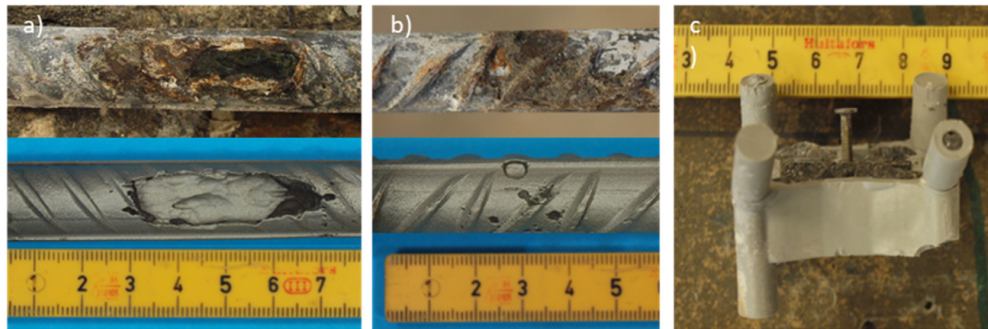


**Fig. 12.** a) Severe pitting corrosion at a spacer in the tidal zone of Beam B (location at around 110 cm at Line 2), cleaned and uncleaned; b) Distributed pitting at a spacer in the tidal zone of Beam E (location at around 160 cm at Line 2), cleaned and uncleaned; c) Representative plastic spacer removed from beam B showing a nail in the middle with potential contact to the reinforcement.

was characterised by high chloride content, low resistivity, and not close to a spacer. In an extensive review, Angst et al. [34] pointed out that large variations are observed in chloride thresholds for corrosion initiation. For Norwegian coastal bridges, a chloride

threshold at 0.72% chloride by weight of cement was suggested by Fluge [35] based on a survey on coastal bridges. This compares to 0.12, 0.12, and 0.14% chloride by weight of concrete for B, E and F, respectively (assuming composition as in Table 1 and 4% air con-



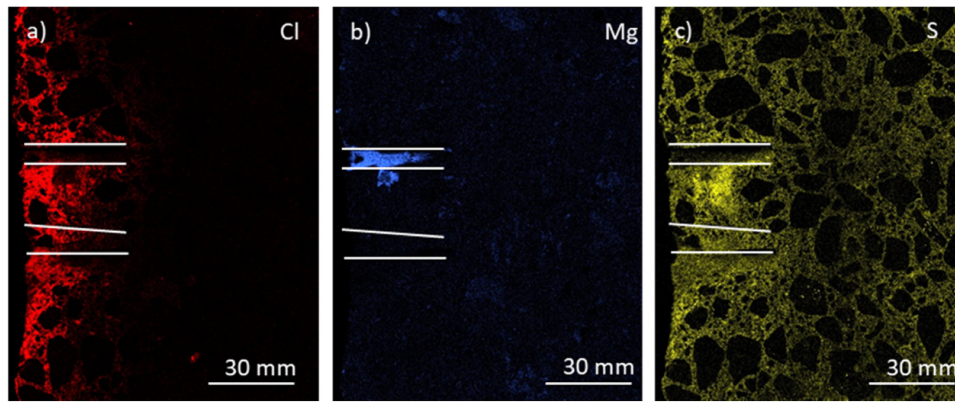


Fig. 13.  $\mu$ -XRF elemental mapping of chloride (Cl), magnesium (Mg) and sulphur (S) at spacers and in surrounding concrete. Beam B (location at around 110 cm at Line 2).

tent). With a concrete cover of 25 mm, this threshold values have been surpassed by a factor of 5–6 in the submerged zone of Beam B and Beam F, while the measured chloride concentrations are below the threshold in Beam E and the tidal and atmospheric zones of Beam F. The chloride contents at more than 0.35% chloride by weight of dry concrete measured at the depth of the reinforcement in the uncracked bulk concrete would, based on [35], indicate “heavy corrosion and pitting”.

### 5.2. Corrosion at cracks

All beams had a substantial number of transverse cracks with typically 10–15 cm distance (see Fig. 14). The large frequency is based on literature expected to reduce the corrosion rate at the individual cracks [1]. Several of the cracks coincided with spacers (Fig. 14), which is expected to make the reinforcement more susceptible to corrosion at these places.

Corrosion at cracks is suggested to be facilitated by (i) rapid initial ingress and (ii) possible wetting and drying [6], but limited by (iii) possible self-healing and (iv) ongoing corrosion at other places (here the spacers) causing cathodic polarization and thus increased chloride threshold, see e.g. [36]. Increased chloride ingress at cracks was observed and the small cover depth of 25 mm suggests moisture variations at the reinforcement (see e.g. [37]), both factors which are expected to facilitate corrosion. Observations in all three beams of extensive precipitation of solids (self-healing) in cracks of width up to 0.2 mm, and in some cases wider, indicate that a possible short-term impact of most of the cracks on transport might have ceased [9]. In addition, precipitation of ettringite on the reinforcement near the cracks was observed (see Fig. 7), which indicates a high pH (10.5–13) [38] that might have provided some long-term protection of the steel. However, the observation of very limited corrosion at other places than spacers despite a high chloride content suggests sustained corrosion at these “weak spots” and cathodic polarization of the surrounding reinforcement as the most likely explanation for the observed limited corrosion at the cracks and on the reinforcement embedded in the bulk. This is in line with the preventive/protective mechanism described by Sagüés and co-workers [36,39,40]. Sagüés et al. [36] suggested a mathematical expression of the influence of polarisation of the steel potential, while in its passive state, on the chloride threshold:

$$C_T = C_{T0} \text{ for } E_S \geq E_{T0} \quad (1)$$

$$C_T = C_{T0} 10^{(E_S - E_{T0})/\beta_{CT}} \text{ for } E_S < E_{T0} \quad (2)$$

where  $C_T$  is the chloride threshold and  $E_S$  is the potential of the steel while still in passive state,  $C_{T0}$  is the initial chloride threshold at the baseline potential,  $E_0$ , and  $\beta_{CT}$  the characteristic inverse slope of  $C_T$  with respect to  $E_S$  when plotted in a  $\log C_T(E_S)$  representation ( $\beta_{CT} = 0.16$  V/dec based on literature data [36]). Applying these potential-dependent chloride thresholds (Eqs. (1) & (2)), Sagüés et al. [36] found that the impact of cathodic polarisation of passive steel by adjacent corroding areas can be quite substantial and affect not only the predicted service life, but also the predicted damage progression trends which may impact structural design decisions to control corrosion.

This suggestion of preventive/protection provided by neighbouring corrosion spots is supported by Fig. 15, where calculated average corrosion rates are plotted as a function of the distance to the nearest major corrosion spot. Not considering the corrosion in Beam E significant, major corrosion spots are observed minimum 1 m apart. The distance of “mutual protection” appears to be 1 m in Beam F and almost 2 m in Beam B (Fig. 15a). Normalising the distance by multiplying with the resistivity indicates a threshold around  $5 \cdot 10^3$  k ohm cm<sup>2</sup> (Fig. 15b).

### 5.3. Corrosion at spacers

High corrosion rates were only observed at spacers in the tidal and submerged zone; but not at all spacers. Corrosion at spacers is assumed to be due to a combination of (i) rapid ingress of chlorides through an inhomogeneous and porous microstructure at the spacers [41,42], (ii) a low(er) chloride threshold at spacers due to inhomogeneities and moisture variation at the steel–concrete interface as well as leaching causing a reduced pH [6], and (iii) sustained corrosion at spacers due to the mentioned inhomogeneities in combination with aggressive environment, which based on the observed corrosion spots appears to be in the tidal zone (Figure 16).

The observations of a detrimental impact of inadequate spacers is supported by Tang and Utgenannt [43]. Investigating chloride-induced corrosion in uncracked concrete slabs after 13 years of marine exposure, Tang and Utgenannt [43] found that in half of the cases the highest corrosion rate occurred at or near the interface between concrete and mortar spacers.

The detrimental impact of the spacers was limited in Beam E and significantly less here than in the two other beams. Microstructural analyses indicated no major differences in phase assemblage between the concretes in Beam E and Beam F, whereas the phases in beam E differed and reflected the higher aluminium content of the binder [9,16]. Visually, all beams were well compacted.

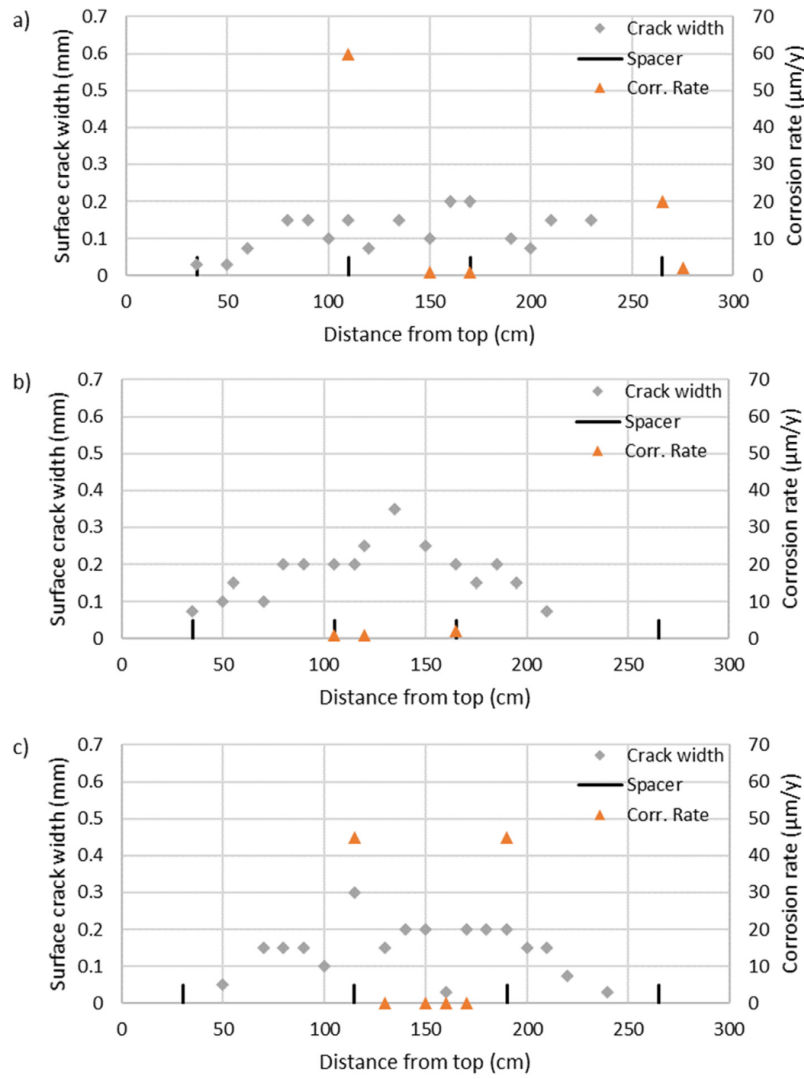


**Fig. 14.** Location of cracks, spacers and observed corrosion for a) Beam B, b) Beam E and c) Beam F. Maximum surface crack width indicated for each crack and estimated average corrosion rate (see text and [Appendix 4](#) for further information).

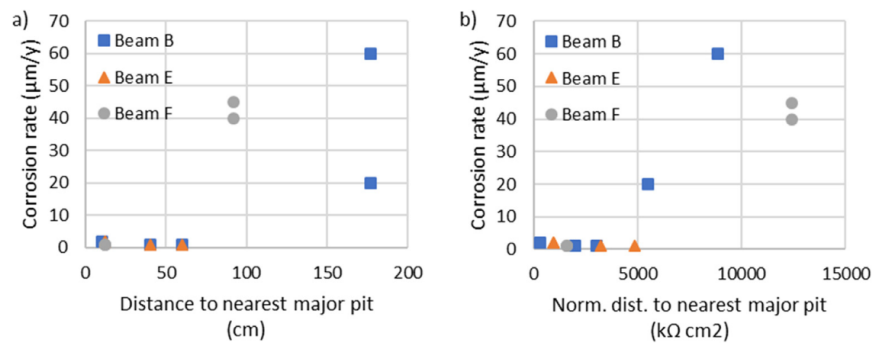


**Fig. 15.** Calculated average corrosion rate ([Appendix 4](#)) versus a) distance to nearest major corrosion spot and b) distance to nearest major corrosion spot normalized by multiplying with the resistivity ( $\rho_{\text{core}}$ ) measured on cores from the tidal zone (except for the two corrosion spots in the submerged zone of Beam B, where the distance was normalized with  $\rho_{\text{core}}$  from this zone). Note that as indicated by the corrosion rates “major corrosion spot” varies between beams (low for Beam E, higher for Beams B and F).

A higher number of larger voids was observed in Beam E compared to Beam B and Beam F, also at the steel–concrete interface. The voids were spread randomly and there was no apparent impact of the casting direction. Full imprints of the reinforcement were observed indicating absence of bleeding (photos can be found in the data report prepared by Danner et al. [21]). Possible explanations for observing less corrosion in Beam E could be (i) the generally lower chloride content (see Fig. 3), (ii) the apparent lower degree of capillary saturation (DCS), (iii) the expected limited leaching because of the lower DCS, and (iv) the higher surface resistivity ( $\rho_{\text{beam}}$ ) of Beam E compared to Beam B and Beam F and higher bulk resistivity ( $\rho_{\text{core}}$ ) compared to Beam B. It should be noted, that there is no general relationship between corrosion rate and concrete resistivity as all three (anodic, cathodic and ohmic) partial corrosion processes affect the rate of active corrosion [44].

#### 5.4. Perspectives

Reviews [1–4] have indicated a need for detailed long-term data and understanding of mechanism of corrosion propagation of steel reinforcement embedded in cracked concrete.

Due to the observed impact of the plastic spacers used on the corrosion performance of the adjacent steel, this study cannot be used for making any general statements on the role of cracks, except that the impact of cracks might be very case specific due to the presence or absence of weaker links. Considering this, we suggest that part of the non-conclusive observations made in the field might be due to other factors than cracks creating weak spots. Potential weak spots facilitating chloride induced corrosion were recently discussed in a review prepared by RILEM TC 262 SCI (steel–concrete interface) [6]. Besides cracks, other macroscopic interfacial concrete voids at the steel–concrete interface as settlement and bleeding zones, and other characteristics as spacers, tie wires, rebar intersections, and welding spots should both be considered when designing and inspecting structures, and when setting up research studies and field exposure sites. Furthermore, monitoring of instrumented rebars in cracked concrete elements exposed in Rødby harbour, Denmark, indicate slow (1–2 years) cycles of de-passivation and re-passivation of steel in submerged and splash marine zones [45]. The investigations are ongoing and not yet supported by destructive investigations. The observations of cyclic behaviour stress the need for not only investigation of long-term exposed structures, but long-term monitoring of corrosion behaviour and other relevant materials and exposure parameters to provide improved understanding of the underlying mechanisms.

To support design and assessment of civil infrastructure in harsh environment with long design life, field exposure data from high quality concrete using high quality spacers, e.g. spacers from high quality mortar, and relevant concrete cover [46] as well as high quality construction methods [47] are needed. Such concerns are reflected in NPRA's recently established exposure site, Field

Station Austefjorden near Bergen, focuses on continuous long-term monitoring [48].

## 6. Conclusions

In 25 years old marine exposed pre-cracked concrete elements, increased chloride ingress was observed at cracks. Severe corrosion was observed in connection with some of the spacers, whereas none or negligible corrosion was observed at cracks not in contact with spacers. It is hypothesised that corrosion at the “weakest link” (here the severely exposed reinforcement at plastic spacers) protects the steel in other areas including at cracks.

Three concrete compositions were investigated, one in accordance with today's NPRA requirements (OPC + 4% SF + 20% FA), one used during the 80's and 90's (OPC + 4% SF) and a more extreme composition (OPC + 12% SF). Fly ash (FA) appears to substantially improve the resistance to chloride and moisture ingress. Comparing to the chloride thresholds typically used, the level of corrosion in the beams with high chloride ingress was very limited.

The present study illustrates the limited importance of cracks in the presence of preventive/protective action from weaker spots. The study does, however, not confirm that cracks are of limited importance if they present the weakest link. Additional long-term studies of cracked structural elements with adequate spacers not providing weak spots are needed to deliver further understanding of the mechanisms and factors controlling the state of the reinforcement. Such knowledge is required to support standardization and preparation of design guides.

## Declaration of Competing Interest

The authors declare that they have no known competing financial interests or personal relationships that could have appeared to influence the work reported in this paper.

## Acknowledgements

This research was part of the Norwegian Public Roads Administration (NPRA), Norway, “Ferry-free coastal route E39” project. The research was furthermore supported by the Research Council of Norway, Norway through its Center of Excellence funding scheme, project number 262644, PoreLab. NPRA is acknowledged for providing the investigated beams (B, E and F), which were prepared, exposed and tested as part of the internal NPRA project “Kloridbestandig betong, Fase I” (Chloride resistant concrete, Phase I) as well as short and long-term chloride data. Professor Klaartje De Weerd, NTNU, is acknowledged for discussions on the application and interpretation of  $\mu$ -XRF analysis and obtaining funding for the apparatus.

## Appendix 1

**Table A1**

Moisture content per gram of binder at each relative humidity step as well as the duration of each step. Reference at 11%.

Relative humidity	95%	90%	85%	80%	75%	70%	50%	30%	11%
Duration of step (h)	50	22	20	22	25	35	55	55	50
Beam B	0.183	0.178	0.174	0.169	0.165	0.160	0.131	0.048	0
Beam E	0.198	0.192	0.185	0.179	0.171	0.163	0.129	0.044	0
Beam F	0.203	0.197	0.192	0.187	0.182	0.178	0.1503	0.053	0

Appendix 2

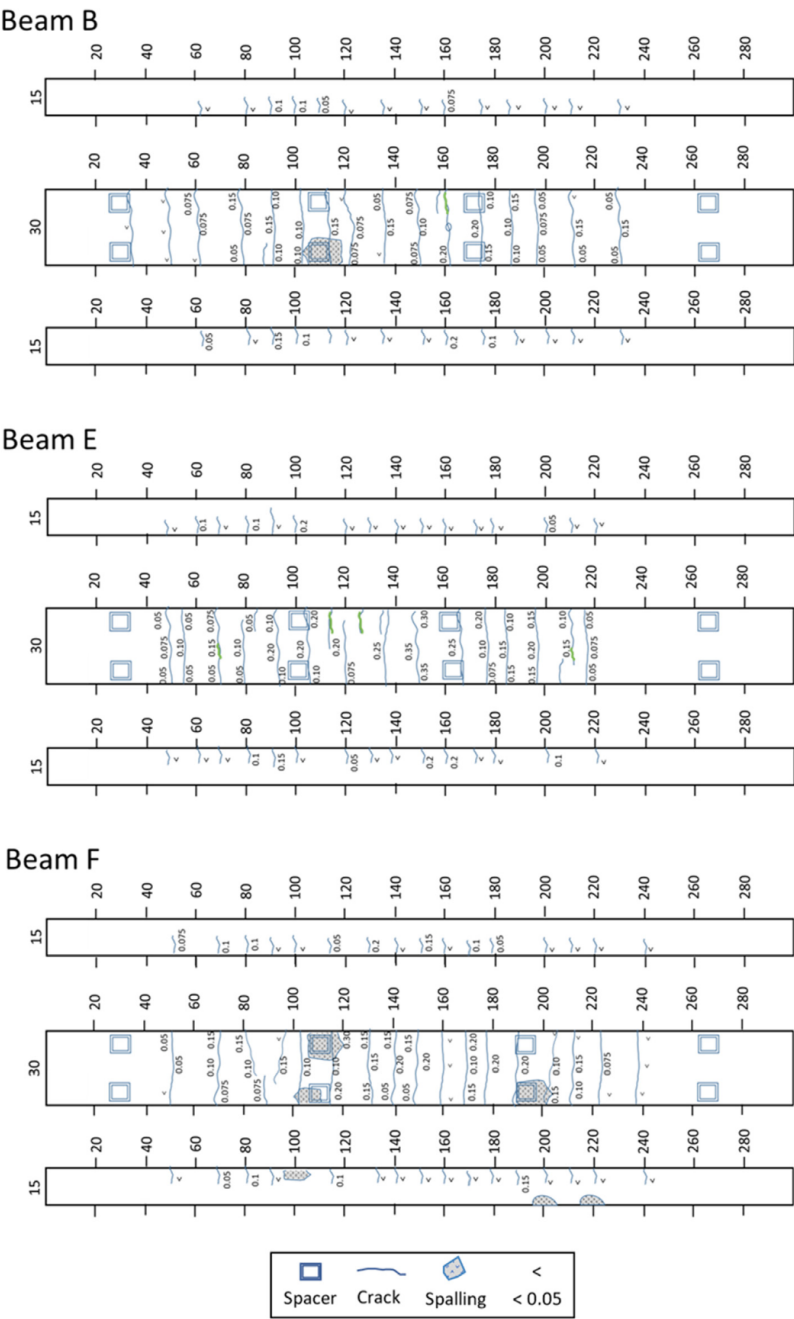
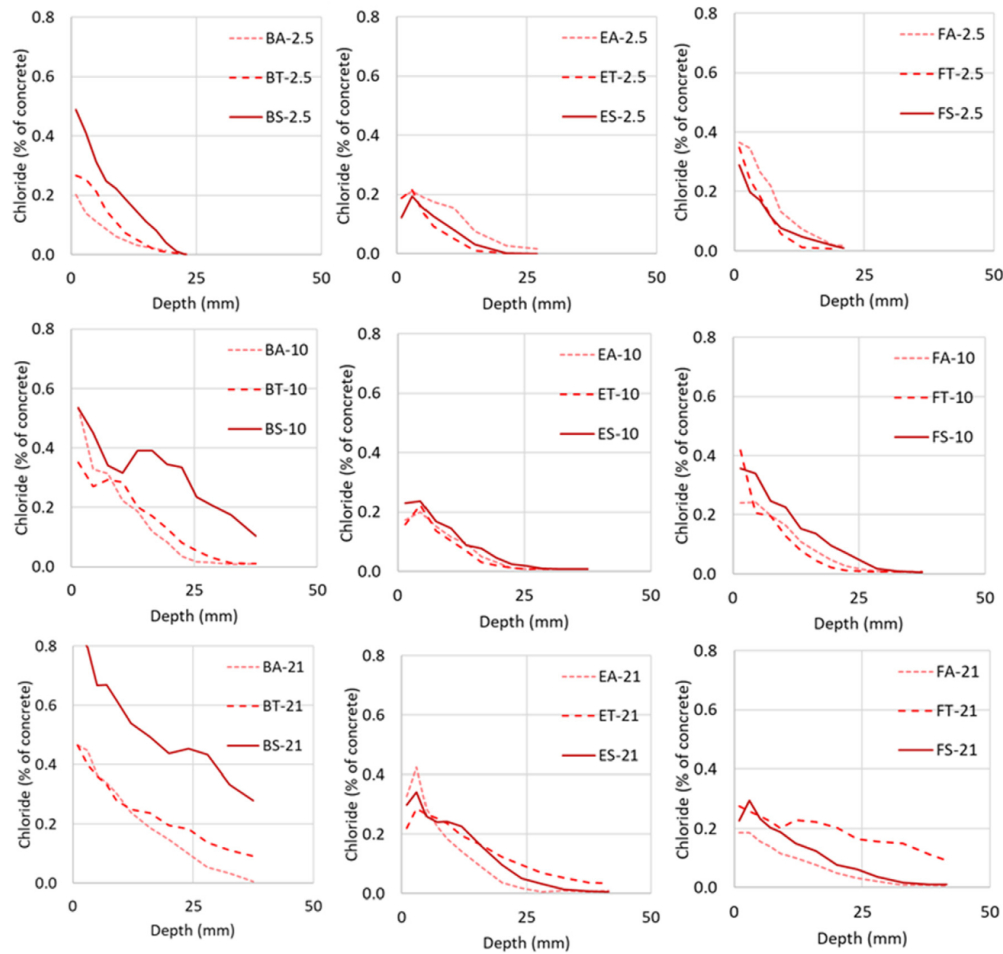


Fig. A2. Visual appearance of beams.



### Appendix 3











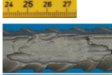


#### Chloride ingress profiles after 2.5, 10 and 21 years



**Fig. A3.** Chloride profiles measured in the atmospheric, tidal and submerged zones of Beam B, Beam E and Beam F after 2.5, 10 and 21 years of exposure. Data courtesy of Norwegian Public Road Administration (NPRA).

## Appendix 4

**Table A4**  
Observed corrosion pits and estimated corrosion rates.

Beam	Location	Geometry (mm)(Length $\pm$ 1 / Depth $\pm$ 0.5)	Picture (after sandblasting)	Estimated average corrosion rate( $\mu\text{m}/\text{year}$ )
B	Line 2, 110 cm(spacer)	44 / 6		$60 \pm 10$
B	Line 2, 150 cm(crack)	Small distributed pitting*		$<1$
B	Line 2, 170 cm(spacer)	Small distributed pitting*		$<1$
B	Line 4, 265 cm(spacer)	27 / 3		$20 \pm 5$
B	Line 4, 275 cm(bulk)	2 / 0.73 / 0.9		$2 \pm 1$
E	Line 2, 100 cm(spacer)	Small distributed pitting*		$<1$
E	Line 2, 160 cm(spacer)	5 / 1		$2 \pm 1$
E	Line 4, 120 cm(crack)	Small distributed pitting		$<1$
E	Line 4, 160 cm(spacer)	14 / 0.9		$2 \pm 1$
F	Line 2, 110 cm(spacer)	Small distributed pitting*		$<1$
F	Line 2, 190 cm(spacer)	48 / 5		$45 \pm 5$
F	Line 4, 110 cm(spacer)	34 / 4.5		$40 \pm 5$
F	Line 4, 190 cm(spacer)	Small distributed pitting*		$<1$

\* Small distributed pitting is defined as corrosion spots with a depth lower than 0.5 mm, which approximately corresponds to a corrosion rate lower than 1  $\mu\text{m}/\text{year}$ .

## References

- [1] A.C.B. Käthler, U.M. Angst, M. Wagner, C.K. Larsen, B. Elsener, Effect of cracks on chloride induced corrosion of steel in concrete - a review, Norwegian Public Roads Administration, NPRA reports, Norwegian Public Roads Administration, Oslo, Norway, 2017, p. 41.
- [2] B.J. Pease, Influence of concrete cracking on ingress and reinforcement corrosion, Department of Civil Engineering, Technical University of Denmark, Kgs. Lyngby, Denmark, 2010. Report: BYG R-233, ISBN: 9788778773128, ISSN: 1601-2917, <https://www.byg.dtu.dk/Forskning/Publicationer/Ph-d-afhandlinger>
- [3] C. Arya, L.A. Wood, S. Alexander, P. Jackson, Technical Report 44 - Relevance of cracking in concrete to reinforcement corrosion Technical Report, The Concrete Society, 2015.
- [4] K. Hornbostel, M. Geiker, Influence of cracking on reinforcement corrosion, in: M. Engen, R. Tan (Eds.), Crack width calculations methods for large concrete structures, Nordic Mini-Seminar, Nordic Concrete Federation, Oslo, Norway, 2017.
- [5] K. Tuutti, Corrosion of steel in concrete, KTH, Kungliga Tekniska Högskolan i Stockholm, Swedish Cement and Concrete Research Institute, Stockholm, ISSN 0346-6906, 1982, p. 468.
- [6] U.M. Angst, M.R. Geiker, M.C. Alonso, R. Polder, O.B. Isgor, B. Elsener, H. Wong, A. Michel, K. Hornbostel, C. Gehlen, R. François, M. Sanchez, M. Criado, H. Sørensen, C. Hansson, R. Pillai, S. Mundra, J. Gulikers, M. Raupach, J. Pacheco, A. Sagüés, The effect of the steel-concrete interface on chloride-induced corrosion initiation in concrete: a critical review by RILEM TC 262-SCI, Mater. Struct. 52 (2019) 88.
- [7] C. Arya, F.K. Ofori-Darko, Influence of crack frequency on reinforcement corrosion in concrete, Cem. Concr. Res. 26 (1996) 345–353.

- [8] W. Ramm, M. Biscop, Autogenous healing and reinforcement corrosion of water-penetrated separation cracks in reinforced concrete, *Nucl. Eng. Des.* 179 (1998) 191–200.
- [9] T. Danner, U. Hjorth Jakobsen, M.R. Geiker, Mineralogical Sequence of Self-Healing Products in Cracked Marine Concrete, *Minerals* 9 (2019) 284.
- [10] T. Danner, M.R. Geiker, On the Influence of Surface and Crack Orientation and Exposure on Ingress in Cracks, *Proceedings of the 72nd RILEM Week 2018 & SLD4, The 4th International conference on service life design for infrastructures, CONMOD2018 International symposium on concrete modelling, Rilem publications*, 2018, p. 600.
- [11] Fédération International du Béton (fib), fib Model Code for Service Life Design - Bulletin 34, Lausanne, Switzerland, 2006, p. 116.
- [12] T. Danner, M.R. Geiker, Long-term Influence of Concrete Surface and Crack Orientation on Self-healing and Ingress in Cracks, *Field Observations* 58 (2018) 1–16.
- [13] J.P. Holtmon, H.R. Isaksen, Utvikling av kloridbestandig betong - Rapport fra produksjon av prøveelementer, Vegdirektoratet, Oslo, Norway, 1994.
- [14] <https://www.tide-forecast.com/locations/Sandnessjoen/tides/latest>, 2017.
- [15] A. Demayo, Elements in sea water, in: D.R. Lide (Ed.) *CRC Handbook of Chemistry and Physics*, CRC Press, U.S.A., 1992.
- [16] U.H. Jakobsen R. No 829235, Microscopy of phases formed in cracks of 25 years old seawater exposed concrete Danish Technological Institute (DTI) 2018 Taastrup, Denmark
- [17] J.P. Holtmon, H.R. Isaksen, Utvikling av kloridbestandig betong - Raåpport fra produksjon av prøveelementer, Vegdirektoratet, Oslo, Norway, 1994.
- [18] K. De Weerd, D. Orsáková, A.C.A. Müller, C.K. Larsen, B. Pedersen, M.R. Geiker, Towards the understanding of chloride profiles in marine exposed concrete, impact of leaching and moisture content, *Constr. Build. Mater.* 120 (2016) 418–431.
- [19] Vegdirektoratet, Retningslinje, Håndbok R211 Feltundersøkelser Oslo, Norway, 2014.
- [20] R. Vegdirektoratet, Håndbok R210, Laboratorieundersøkelser, Oslo, Norway, 2016.
- [21] T. Danner, A.B. Revert, M.R. Geiker, Field Station Sandnessjøen - Effect of cracks in concrete, Data report Report 374, Statens vegvesens rapporter, Statens vegvesen (Norwegian Public Roads Administration), Trondheim, 2020.
- [22] R.B. Polder, Test methods for on site measurement of resistivity of concrete - a RILEM TC-154 technical recommendation, *Constr. Build. Mater.* 15 (2001) 125–131.
- [23] T. Danner, K. Hornbostel, K. De Weerd, M.R. Geiker,  $\mu$ -XRF-characterisation of chloride ingress and self-healing in cracked concrete, *NORDIC CONCRETE RESEARCH. Proceedings of the XXIII Nordic Concrete Research Symposium, Norsk Betongforening, Trondheim/Fornebu*, 2017, pp. 372.
- [24] J. Lindgård, E.J. Sellevold, M.D.A. Thomas, B. Pedersen, H. Justnes, T.F. Rønning, Alkali-silica reaction (ASR)—performance testing: Influence of specimen pre-treatment, exposure conditions and prism size on concrete porosity, moisture state and transport properties, *Cem. Concr. Res.* 53 (2013) 145–167.
- [25] Vaisala, HM44 Datasheet B211768 EN-A - Vaisala, 2018.
- [26] D.R. Williams, The characterisation of powders by gravimetric water vapour sorption, *Int. LABMATE* 20 (6) (1995) 40–42.
- [27] L. Wadsö, A. Anderberg, I. Åslund, O. Söderman, An improved method to validate the relative humidity generation in sorption balances, *Eur. J. Pharm. Biopharm.* 72 (2009) 99–104.
- [28] O. Linderöth, P. Johansson, L. Wadsö, Development of pore structure, moisture sorption and transport properties in fly ash blended cement-based materials, *Constr. Build. Mater.* 261 (2020) 120007.
- [29] R.F. Feldman, V.S. Ramachandran, Differentiation of interlayer and adsorbed water in hydrated portland cement by thermal analysis, *Cem. Concr. Res.* 1 (1971) 607–620.
- [30] R.F. Feldman, V.S. Ramachandran, A study of the state of water and stoichiometry of bottle-hydrated  $\text{Ca}_3\text{SiO}_5$ , *Cem. Concr. Res.* 4 (1974) 155–166.
- [31] R.F. Feldman, P.J. Sereda, A model for hydrated Portland cement paste as deduced from sorption-length change and mechanical properties, *Matériaux et Construction* 1 (1968) 509–520.
- [32] O. Linderöth, P. Johansson, A method to determine binder content in small samples of cementitious material using hydrochloric acid and ICP-OES analysis, *Mater. Today Commun.* 20 (2019) 100538.
- [33] K. Hornbostel, U. Angst, C.K. Larsen, Field testing after 16 years exposure, Solsvik feltstasjon - prøving av betong i marint miljø, Statens vegvesens rapporter No. 675, Statens vegvesen (Norwegian Public Roads Administration), Oslo, Norway, 2020.
- [34] U. Angst, B. Elsener, C.K. Larsen, Ø. Vennesland, Critical chloride content in reinforced concrete - a review, *Cem. Concr. Res.* 39 (2009) 1122–1138.
- [35] Finn Fluge, Marine chlorides - A probabilistic approach to derive provisions for EN 206-1, in: Fluge (Edts), Service life design of concrete structures, Betongkonstruksjoners livsløp, Report 19, Norwegian Public Roads Administration, Oslo, Norway, 2003. ISBN 82-91228-25-6.
- [36] A.A. Sagüés, A.N. Sánchez, K. Lau, S.C. Kranc, Service Life Forecasting for Reinforced Concrete Incorporating Potential-Dependent Chloride Threshold, *CORROSION* 70 (2014) 942–957.
- [37] U.M. Angst, M.R. Geiker, A. Michel, C. Gehlen, H. Wong, O.B. Isgor, B. Elsener, C. M. Hansson, R. Francois, K. Hornbostel, R. Polder, M.C. Alonso, M. Sanchez, M.J. Correia, M. Criado, A. Sagues, N. Buenfeld, The steel/concrete interface, *Mater. Struct.* 50 (2017) 24.
- [38] D. Damidot, F.P. Glasser, Thermodynamic investigation of the  $\text{CaO-Al}_2\text{O}_3\text{-CaSO}_4\text{-H}_2\text{O}$  system at 25°C and the influence of  $\text{Na}_2\text{O}$ , *Cem. Concr. Res.* 23 (1993) 221–238.
- [39] M.T. Walsh, A.A. Sagüés, Steel Corrosion in Submerged Concrete Structures—Part 1: Field Observations and Corrosion Distribution Modeling, *CORROSION* 72 (2016) 518–533.
- [40] M.T. Walsh, A.A. Sagüés, Steel Corrosion in Submerged Concrete Structures—Part 2: Modeling of Corrosion Evolution and Control, *CORROSION* 72 (2016) 665–678.
- [41] S. Alzyoud, Effect of reinforcement spacers on concrete microstructure and durability, *Civil and Environmental Engineering* Imperial College London, 2015, p. 182.
- [42] S. Alzyoud, H.S. Wong, N.R. Buenfeld, Influence of reinforcement spacers on mass transport properties and durability of concrete structures, *Cem. Concr. Res.* 87 (2016) 31–44.
- [43] L. Tang, P. Utgenannt, A field study of critical chloride content in reinforced concrete with blended binder, *Mater. Corros.* 60 (2009) 617–622.
- [44] K. Hornbostel, B. Elsener, U.M. Angst, C.K. Larsen, M.R. Geiker, Limitations of the use of concrete bulk resistivity as an indicator for the rate of chloride-induced macro-cell corrosion, *Structural Concrete* 18 (2017) 326–333.
- [45] A. Michel, H.E. Sørensen, M.R. Geiker, 5 years of in situ reinforcement corrosion monitoring in the splash and submerged zone of a cracked concrete element, *Construction & Building Materials* 285 (2021), 122923.
- [46] S. Rostam, High performance concrete cover—why it is needed, and how to achieve it in practice, *Constr. Build. Mater.* 10 (1996) 407–421.
- [47] M.R. Geiker, On the importance of execution for obtaining the designed durability of reinforced concrete structures, *Materials and corrosion - Werkstoffe und Korrosion* 63 (2012) 1114–1118.
- [48] K. Hornbostel, B. Pedersen, Austefjorden feltstasjon - prøvning av betong i marint miljø, SVV rapporter No. 494, Statens vegvesen / Norwegian Public Roads Administration, 2020.